The ^{2}H($\vec{p},\gamma$)^{3}He and ^{1}H($\vec{d},\gamma$)^{3}He reactions below 80 keV

G. J. Schmid,[1,2,*] B. J. Rice,[1,2] R. M. Chasteler,[1,2] M. A. Godwin,[1,2] G. C. Kiang,[3] L. L. Kiang,[4] C. M. Laymon,[1,2]
R. M. Prior,[5] D. R. Tilley,[1,6] H. R. Weller[1,2]
[1]*Department of Physics, Duke University, Durham, North Carolina 27708*
[2]*Triangle Universities Nuclear Laboratory, Duke Station, Durham, North Carolina 27708*
[3]*Academia Sinica, Taipei, Taiwan*
[4]*National Tsing-Hua University, Taipei, Taiwan*
[5]*Department of Physics, North Georgia College, Dahlonega, Georgia 30597*
[6]*North Carolina State University, Raleigh, North Carolina 27695*

(Recevied 4 June 1997)

The details of a recent experimental study of the ^{2}H($\vec{p},\gamma$)^{3}He and the ^{1}H($\vec{d},\gamma$)^{3}He reactions for beam energies below 80 keV are discussed. In this study, both polarized and unpolarized incident beams were used to measure the cross section $\sigma(\theta,E)$, the astrophysical S factor $S(\theta,E)$, the vector analyzing power $A_y(\theta,E)$, and the tensor analyzing power $T_{20}(\theta)$. In addition, the γ-ray linear polarization $P_\gamma(\theta)$ was measured for an unpolarized incident beam. The experimental details of these measurements are discussed and the data are analyzed to obtain the amplitudes and phases of the contributing transition-matrix elements. The results of our measurements are compared with recent *ab initio* three-body theoretical calculations. This comparison reveals the large sensitivity of the polarization observables, especially the vector analyzing power (A_y), to the presence of meson-exchange current effects and indicates the need for further study. The tensor analyzing power data [$T_{20}(\theta)$] are used to extract a value of the asymptotic D- to S-state ratio, η, for ^{3}He. [S0556-2813(97)03511-5]

PACS number(s): 21.45.+v, 24.70.+s, 25.10.+s, 25.40.Lw

I. INTRODUCTION

This paper details the motivations, procedures, and conclusions of a set of recent ^{2}H($\vec{p},\gamma$)^{3}He and ^{1}H($\vec{d},\gamma$)^{3}He experiments at low energies ($E_{\mathrm{c.m.}} < 53$ keV), and compares the results with current theoretical work in three-body nuclear physics. The relationship to and possible impact on nuclear astrophysics is also discussed. Some results of our work have already been published [1–3], but here we provide a detailed presentation of the acquisition and analysis of the data which is necessary to fully understand our results and justify our conclusions.

As discussed in Ref. [1], these reactions are particularly interesting at low energies for two reasons: first, to allow testing of theoretical three-body work which has been done below neutron production threshold and below the Coulomb barrier; and second, to explore issues related to nuclear astrophysics. We explore each of these topics in detail in the next two subsections. A discussion of experimental procedure and a presentation of results follows.

A. Three-body nuclear physics

Some specific aspects of three-body nuclear physics which are of current interest include the treatment of Coulomb and meson-exchange current (MEC) effects. The first exact treatment of the Coulomb effect in the three-body system was done at thermal energies (essentially zero energy) by Friar *et al.* in 1991 [4], but this has recently been extended to finite energies [5]. In addition to the Coulomb interaction there is the question of the accuracy with which the explicit MEC's can be treated in the current NN potential models. It has been known for years that calculations of the n-d capture cross section near zero energy are off by a factor of about 2 if MEC effects are not included [6]. Similarly, the ^{2}H(p,γ)^{3}He and ^{1}H(d,γ)^{3}He reactions are sensitive to MEC effects, especially at very low energies as discussed below.

The diagram in Fig. 1 shows the four dominant couplings (in the channel-spin scheme) which can be expected in the

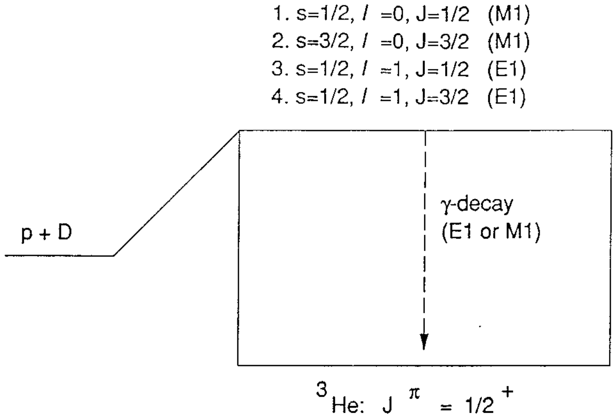

FIG. 1. Energy level diagram representing the p-d capture process. The p-d system, with $E_{\mathrm{c.m.}} < 53$ keV, captures into a ^{3}He continuum state ($E_x \sim E_{\mathrm{c.m.}} + Q$) which then decays by gamma emission. The four dominant TME's are shown by the quantum numbers s, ℓ, and J.

---

[*] Present address: Lawrence Berkeley National Laboratory, Berkeley, CA 94720.

^{2}H$(p,\gamma)^3$He reaction at low energies once we decompose the electromagnetic operator into multipoles. Since the ^{3}He ground state is positive parity, we see that the s-wave ($\ell=0$) continuum states decay via $M1$ or $E2$ radiation while the p-wave ($\ell=1$) continuum states decay via $E1$ radiation. At the low energies of the current experiment we expect s-wave $M1$ and p-wave $E1$ radiation to dominate.

The presence of a substantial amount of $M1$ radiation is responsible for the MEC sensitivity. Due to Siegert's theorem, the electric multipoles can be handled without explicit reference to meson-exchange currents. However, this is not true for the magnetic multipoles, and hence a calculation of the $M1$ strength requires explicit reference to the MEC effects. The $M1$ operator can be written as a combination of MEC and impulse approximation (IA) components [6,7]. Typically, the IA part is much larger than the MEC part (e.g., in n-p capture) and hence the MEC sensitivity is lost. In n-d and p-d capture, however, the IA part is greatly suppressed because the symmetric S state, the dominant part of the ^{3}H and ^{3}He ground states, is an eigenfunction of the IA M1 operator [8,9]. This leads to the supposition that at low energies the ^{2}H$(p,\gamma)^3$He reaction should proceed largely by MEC driven $M1$ (since the associated two-body current operators do connect the dominant S-state components) and hence should be a good place to test our theoretical understanding of the treatment of MEC effects. Since a set of three-body calculations which include MEC as well as Δ-isobar effects have recently been completed at these low energies [2], we see immediately the usefulness of an accurate ^{2}H$(p,\gamma)^3$He and ^{1}H$(d,\gamma)^3$He data set.

The arguments given for studying MEC effects via ^{2}H$(p,\gamma)^3$He hold equally well for ^{2}H$(n,\gamma)^3$H. In fact, the absence of both Coulomb effects and $E1$ radiation have resulted in more theoretical studies being devoted to the ^{2}H$(n,\gamma)^3$H reaction than ^{2}H$(p,\gamma)^3$He. One advantage of the ^{2}H$(p,\gamma)^3$He system, however, is that the presence of p waves at $E=0$, a result of the Coulomb interaction, leads to analyzing power effects which are absent in the n-d system. For energies slightly above $E=0$ we can measure polarization observables in ^{2}H$(\vec{p},\gamma)^3$He and ^{1}H$(\vec{d},\gamma)^3$He and expect large effects.

B. Nuclear astrophysics

The ^{2}H$(p,\gamma)^3$He reaction plays an important role in nuclear astrophysics, both in stellar and protostellar evolution. In stellar evolution, the ^{2}H$(p,\gamma)^3$He reaction forms the second step in the proton-proton chain [10], which is the sequence of nuclear reactions which fuels low to medium mass stars like our sun. The temperature of the sun's core is about 15 million K, which corresponds to a center-of-mass energy of about 1 keV. Although the ^{2}H$(p,\gamma)^3$He reaction is prominently featured as the second step on the proton-proton chain, it is important to note that it follows a weak interaction (p-p fusion) in the sequence. This effectively bottlenecks the p-d capture process, and thus ensures that experimental knowledge of the p-d capture rate is essentially unimportant for calculations dealing with energy generation in the sun. As pointed out in Ref. [1], this indicates that the generation of solar neutrinos (especially in the p-^{7}Be capture process which follows the p-d and α-^{3}He capture steps) will be unaffected by deuterium burning, and hence the "solar neutrino problem" [10] will not be affected by studying solar p-d capture.

Although the p-d reaction rate is unimportant for typical stellar evolution calculations, it turns out to be very important for calculations dealing with protostellar evolution. As discussed by Stahler [11], the ^{2}H$(p,\gamma)^3$He reaction is the first nuclear reaction to ignite in a developing protostar (at a temperature of about 1 million K, or $E_{\text{c.m.}}$ about 0.1 keV). The deuterium that is burned in this case is primordial deuterium (deuterium created in the Big Bang) instead of weakly generated p-p deuterium. This freedom from the p-p bottleneck allows p-d fusion to exert a strong influence on protostellar development. The specific effect of the p-d burning is to cause the protostar to expand as it accretes mass, and thereby maintain a constant temperature in the core (the "thermostat effect"). This leads to observable effects on the protostellar development as discussed in [11].

C. Astrophysical S factor

At the low energies of astrophysical interest, charged particle cross sections are greatly inhibited by the Coulomb barrier, which causes them to fall exponentially with decreasing beam energy. This yields low experimental count rates which often make it necessary to measure the cross section at somewhat higher energies, and then to extrapolate the results downward. This extrapolation procedure involves parameterizing the cross section at low energies in terms of known energy dependencies, namely Coulomb barrier penetration and "geometrical" cross section effects. The remaining energy dependence, the so-called "astrophysical S factor," varies only slowly with energy and is, one hopes, easier to extrapolate than the cross section. The cross section is defined in terms of the S factor, $S(E_{\text{c.m.}})$, as follows [10]:

$$\sigma(E_{\text{c.m.}})=\frac{S(E_{\text{c.m.}})e^{-2\pi\eta}}{E_{\text{c.m.}}}, \tag{1}$$

where η is the Sommerfeld parameter. For the p-d capture process, η is related to the center-of-mass energy as follows:

$$2\pi\eta=\frac{25.639}{E_{\text{c.m.}}}, \tag{2}$$

where $E_{\text{c.m.}}$ is in keV.

D. Previous $d(p,\gamma)^3$He work

In the very low energy region of interest, the only previous ^{2}H$(p,\gamma)^3$He data taken is that of Griffiths *et al.* [12]. At slightly higher energies, the data set of Bailey *et al.* [13] also exists. Figure 2 shows the S-factor results of Griffiths *et al.*, where the open points represent the actual data and the dashed line represents a theoretical energy dependence (the direct capture model) normalized to the data. From the standpoint of protostellar evolution, we are interested in the ^{2}H$(p,\gamma)^3$He reaction rate at energies less than 1 keV, and thus the extrapolation via the dashed line takes on considerable importance. The key thing to note from Fig. 2 is that the energy dependence is not experimentally determined. Although the data points could be said to be consistent with the

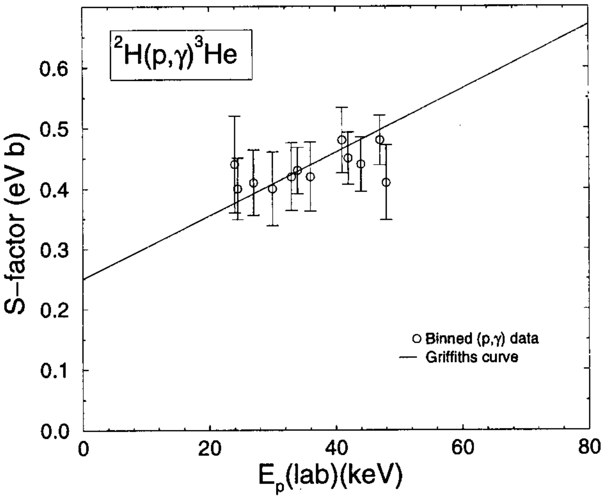

FIG. 2. The *S*-factor data of Ref. [12]. The dashed line represents the energy dependence of a direct capture model which has been normalized to the data by an overall multiplicative constant.

dashed line, they certainly do not uniquely define such a line. Better experimental confirmation of this energy dependence would be desirable, and this constitutes one of the motivations for the current ^{2}H$(p,\gamma)^3$He study.

E. Goals of the current $d(p,\gamma)^3$He and $p(d,\gamma)^3$He studies

One of the goals of the current ^{2}H$(p,\gamma)^3$He study was to measure the absolute value of the S factor (or equivalently, the cross section) in the low energy region ($E_{\mathrm{c.m.}} < 53$ keV, or, in the lab frame, $E_p < 80$ keV). This information is valuable to theorists in both three-body physics and astrophysics, as discussed above. In addition, we wanted to use polarization observables in order to extract detailed information about the amplitudes and phases of the contributing $E1$ and $M1$ transition-matrix elements.

The advantages that the current experiment had over all previous low energy ^{2}H$(p,\gamma)^3$He experiments were the use of a large high-purity germanium (HPGe) detector and the use of a high intensity polarized proton beam. The resolution of the HPGe detector, which is much better than that of the NaI(Tl) detectors used in previous experiments, provided improved separation of background radiation. This superior resolution also enabled us to extract the energy dependence of the ^{2}H$(p,\gamma)^3$He reaction directly from the thick target spectra (see Sec. III). The polarized incident beams used in this experiment allowed us to measure the vector analyzing power, $A_y(\theta,E)$, which is very sensitive to $E1/M1$ mixing. By measuring this quantity we hoped to determine the relative roles of $E1$ and $M1$ capture in the ^{2}H$(p,\gamma)^3$He reaction below $E_p = 80$ keV.

Other improvements that the current experiment made upon the previous work were that significantly more data were acquired (improving the counting statistics) along with detailed angular distributions [the cross section was previously [12] assumed to be of the form $\sigma(\theta) = \sin^2\theta + \mathrm{const}$]. One final improvement that we introduced in the current experiment was that we measured the γ-ray linear polarization, $P_\gamma(\theta)$. Although this measurement has been previously done for ^{2}H$(p,\gamma)^3$He at higher energies [14], it had not been measured in the very low energy region of the present experiment.

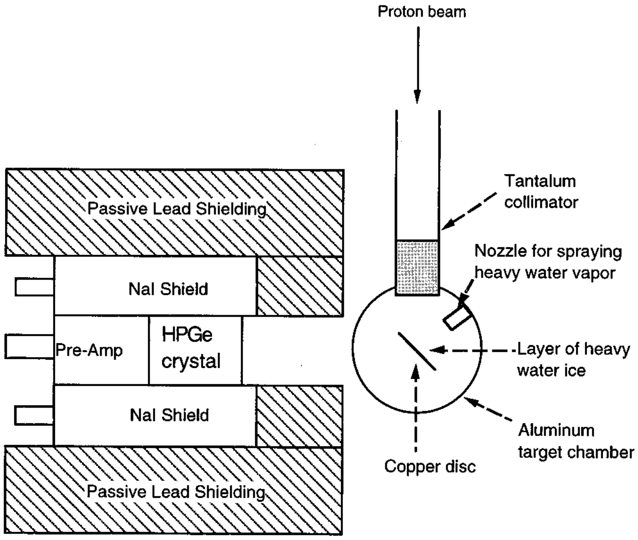

FIG. 3. The physical setup of the current ^{2}H$(p,\gamma)^3$He experiment. The 80 keV proton beam is incident on a heavy water ice target (which has been condensed upon a Cu disc inside the target chamber). The p-d capture γ rays are detected by an actively and passively shielded HPGe crystal (shown here at a lab angle of 90°).

II. EXPERIMENTAL METHODS

In this section we discuss the experimental techniques used to acquire data in the current ^{2}H$(p,\gamma)^3$He and ^{1}H$(d,\gamma)^3$He experiment. This will include a discussion of the physical setup itself, as well as the techniques used to process the signals, to create the D_2O and H_2O ice targets, to integrate the beams, and to measure the HPGe detector efficiency. Experimental details relative to measuring the vector and tensor analyzing analyzing powers and to the γ-ray polarization will also be presented.

A. Physical setup

Figure 3 shows the experimental setup used in the current experiment. The technique used was to stop an 80 keV beam (from an Atomic Beam Polarized Ion Source, ABPIS [15]) of protons or deuterons in an ice target (D_2O or H_2O, respectively). The idea of using ice targets was taken from the work of Griffiths *et al.* [12]. The capture γ rays, at energies of approximately 5.5 MeV, were detected by a HPGe detector that was anticoincidence shielded by a surrounding NaI(Tl) annulus (which was segmented into four separate quadrants). Several inches of lead surrounded the setup on all sides. The target chamber which held the target was constructed of aluminum with walls 1.6 mm thick.

B. Signal processing

The raw signals from the HPGe detector were processed using an electronics setup detailed in Ref. [16]. Figure 4 shows the primary components of this setup. The raw HPGe signals were passed through a preamp and then fanned out to

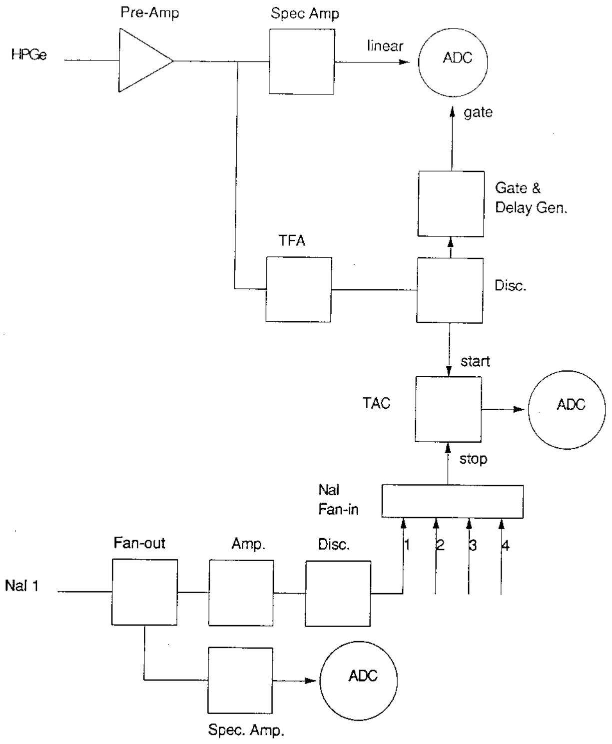

FIG. 4. A diagram showing part of the electronics set up for the current $^2H(p,\gamma)^3He$ experiment. Only one NaI(Tl) segment is shown here (the others being of similar form).

a spectroscopy amplifier (''Spec Amp'') and a timing filter amplifier (TFA) as shown in Fig. 4. The Spec Amp allowed shaping of the linear signal (6 μs shaping time) before it was fed into the ADC. The TFA and subsequent constant fraction discriminator allowed amplification and discrimination of the timing signal which eventually gated the ADC linear signal. The discriminator threshold was typically set at around 500 keV for the HPGe. Before being fed into the ADC, the timing signal was passed through a gate and delay generator to create the proper signal shape, and proper signal width (about 10 μs).

As can be seen in Fig. 4, the timing signal from the HPGe was also fed into a time to amplitude converter (TAC) as the ''start'' signal. The stop signal was an ''or'' of the timing signals from the four separate NaI(Tl) quadrants. The random coincidence (off TAC peak) rate was negligible for this setup.

The electronics setup for one of the four NaI quadrants is shown in Fig. 4. Like the preprocessing for the HPGe detector, the Spec Amps shape the linear signals which were then sent to the ADC. However, unlike the HPGe, the timing signals do not gate the ADC, but instead were only used for the TAC input. The NaI(Tl) signals were actually gated into the ADC by the HPGe timing signals [i.e., only coincidence NaI(Tl) spectra were stored].

The digitized ADC signals from the HPGe and the NaI(Tl) were fed into a CAMAC crate controller which was in turn connected to a MicroVAX 3200 computer by means of a Microprogrammed Branch Driver (MBD). The online data acquisition system was the TUNL XSYS package [17]. When polarized incident beams were used, an additional series of electronic manipulations were done in order that the $^2H(p,\gamma)^3He$ yields associated with different spin states would be routed properly to different spectra. Further details on the spin-flip electronics can be found in Ref. [16].

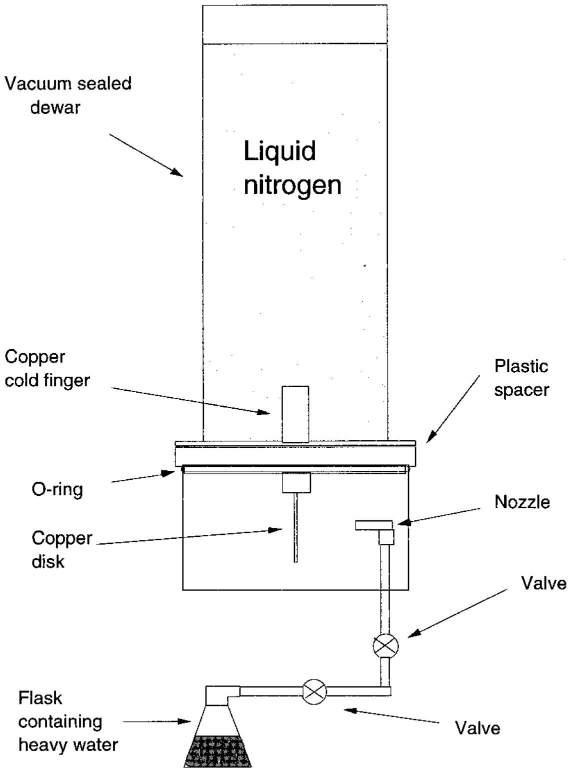

FIG. 5. The target chamber and dewar set up for the current experiment. The D_2O ice target was maintained at liquid nitrogen temperatures by means of the copper cold finger which was in contact with an LN_2 reservoir.

C. Ice targets

For the case of the $^2H(p,\gamma)^3He$ experiment, the proton beam passed through a tantalum collimator before hitting the heavy water ice target (Fig. 3). The D_2O ice target was made by evaporation of heavy water (better than 99% pure) onto a cooled copper disc located in the target chamber. Figure 5 shows the setup of the target chamber and dewar system. Opening the hand valves exposed the flask containing heavy water to the low vapor pressure of the target chamber. This caused the D_2O water in the flask to boil, forming a vapor which passed through the nozzle shown and into the target chamber. The target, a copper disc 1.6 mm thick, was kept in contact with a large liquid nitrogen reservoir via a thick copper cold finger. The copper disc maintained a temperature of approximately 80 K causing the D_2O vapor to condense in ice form on the surface. In this manner, D_2O ice targets of about 0.5 mm in thickness could be fabricated (over the course of about 15 min of deposition).

The purity of the ice target could be gauged over the course of an experiment by monitoring the $^2H(p,\gamma)^3He$ count rate in the HPGe. If impurities built up on the surface (e.g., carbon), a gradual decrease in the count rate would be expected. No such decreases were observed. The durability of these ice targets was quite good. Under 30 μA of proton bombardment, the $^2\mathrm{H}(p,\gamma)^3\mathrm{He}$ count rate in the HPGe would hold steady for several days (on average), before rapidly dying off. This rapid deterioration was due to complete vaporization of the D_2O ice target, at which point a new layer would be deposited.

The physical setup for the the $^1\mathrm{H}(d,\gamma)^3\mathrm{He}$ experiment was the same as for the $^2\mathrm{H}(p,\gamma)^3\mathrm{He}$ runs, except that the beam was composed of deuterons and the liquid evaporated onto the cooled copper disk was distilled H_2O. The initial target deposition time was 15 min, as in the case of the D_2O target. The constant bombardment of deuterons, however, caused a steady increase in the $^2\mathrm{H}(d,n)$ yield and created a background which competed with the 5.5 MeV γ ray of interest. To limit this background layers of H_2O were deposited approximately every six hours.

D. Integrating the beam current

In order to know how many protons were incident on the target it was necessary to integrate the charge deposited on the ice targets. Two potential problems with beam current integration are the following: electrons can be knocked out of the target by the incident beam, and thus create a current reading which is artificially high (for positive incident beam); or electrons can be knocked off the beam-pipe upstream and impinge on the target, creating a current reading which is artificially low. The latter problem was addressed by biasing the upstream collimator to $+90$ V. A test undertaken to address the former problem showed that the integrated current on the ice target was independent of applied target bias (ranging from 0 to 300 V). This result indicates that secondary electrons are not being emitted from the ice target, in agreement with the previous experimental results of Ref. [18].

E. Stopping cross section

In order to calculate the reaction cross section, we also need to obtain the deuterium areal density, D, which is dependent on the stopping cross section, $STP(E)$, for protons on D_2O ice. The stopping cross section is related to D as follows:

$$dD=\frac{2(dE)}{STP(E)}, \tag{3}$$

where dD is the differential deuterium areal density, and dE is the differential energy width of the incident beam. To find the deuterium areal density, D, for the range $E=80-0$ keV, we integrate Eq. (3) over this range. The factor of two in Eq. (3) comes from the fact that there are two deuterium nuclei for each D_2O molecule.

The stopping cross section for protons on D_2O ice is known from measurements by Wenzel *et al.* [19] and Whaling *et al.* [20]. Figure 6 shows, by the solid and open points, the results of these measurements. The solid line is an empirical fit to the data using the form derived by Anderson and Ziegler [21]:

$$E_p<10\mathrm{keV}: \frac{1}{STP(E_p)}=\frac{1}{C_1\sqrt{E_p}}, \tag{4a}$$

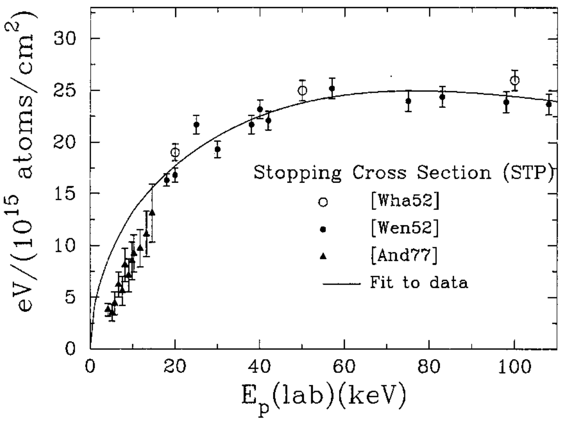

FIG. 6. The stopping cross section data of Refs. [19,20], for protons on D_2O ice, shown along with an empirical fit.

$$E_p>10\mathrm{keV}: \frac{1}{STP(E_p)}=\frac{1}{C_2E_p^{0.45}}+\frac{1}{(C_3/E_p)\ln(1+C_4/E_p+C_5/E_p)}. \tag{4b}$$

The empirical form of Eq. (4) was derived by taking into account both theoretical considerations (concerning electronic stopping) and experimental considerations (i.e., fits to all stopping cross section data acquired as of 1977). A constraint was applied to the constants so as to provide continuity at 10 keV. The extracted constants are $C_1=4.174$, $C_2=4.733$, $C_3=3405$, $C_4=594$, and $C_5=0.0084$.

The experiment of Griffiths *et al.* [12], discussed in Sec. I D, used $STP(E)$ values for protons on H_2O vapor instead of D_2O ice (which was their actual target). Their assumption was that the two values should be the same. However, the values for H_2O vapor and D_2O ice are expected to be different based on the now established "physical state effect" [22,23]. The theoretical basis for the physical state effect [24,25] is that electrons are more tightly bound in the ice phase than they are in the vapor phase, making the stopping cross section smaller in the ice phase. This indicates that the $STP(E)$ values of Griffiths were high by 10–15 %, and thus, based on Eqs. (3) and (5), we see that their cross sections (and S factors) will also be high by 10–15 %.

F. HPGe efficiency curve

The acquisition of an efficiency curve for the current HPGe detector was thoroughly discussed in a recent article [3], and the interested reader is referred there for all the details. To summarize, the efficiency value used in Ref. [1] is too high, and thus the S-factor data presented there is too low. Whereas the value of the S factor obtained in Ref. [1] was about 50% lower than the value of Griffiths *et al.* [12], the corrected value is about 35% lower than that of Ref. [12]. The correct efficiency value, used in the calculations of Refs. [2,3], is $\epsilon=0.095\pm0.006$, where ϵ is the intrinsic photopeak efficiency of the HPGe detector at 5.5 MeV, and the error includes both statistical and systematic contributions.

G. Cross section

Based on the above quantities, the differential reaction cross section for $^2\mathrm{H}(p,\gamma)^3\mathrm{He}$ can be written in terms of the acquired γ-ray photopeak yield $Y(\theta,E_p)$ (where θ is the laboratory angle of the detector and E_p represents the beam energy) as follows:

$$\sigma(\theta,E)=\frac{Y(\theta,E_p)}{(D(E_p))(\epsilon d\Omega)(P)}, \tag{5}$$

where $D(E_p)$ is the deuterium areal density of the target, $\epsilon d\Omega$ is the intrinsic photopeak efficiency times solid angle (in steradians) of the HPGe detector, and P is the number of protons incident on the target (obtained from the beam current integration).

H. Systematic error in the cross section

The total error on the measured cross section will have two components: a statistical component, based solely on counting statistics; and a systematic component based on estimated errors in the procedural techniques. The primary components of the systematic error are the error in the beam current integration, the error in the efficiency measurement, and the error in the stopping cross section curve. To get the total systematic error, we added each of these component errors in quadrature. To obtain the total error on the absolute cross section (or S factor), we then add the statistical and systematic errors in quadrature.

The error on the beam current integration is estimated at 1%. This is due to the fact that secondary electron emission is not thought to be a problem, and that the beam current integrator is known to be accurate to better than 1%. The error on the efficiency measurement at 5.5 MeV is estimated to be 6% based on counting statistics, uncertainties in the strengths of the absolutely calibrated sources, and errors in the fitting and extrapolation procedure (see Ref. [3]). The error in the stopping cross section curve is taken to be 6%, which is the accuracy of the stopping cross section data of Refs. [19,20]. Combined in quadrature, these component errors indicate a total systematic error of 9%.

I. Vector analyzing power

The measurement of the $^2\mathrm{H}(\vec{p},\gamma)^3\mathrm{He}$ vector analyzing power, $A_y(\theta,E)$, was performed using the polarized proton beam from the ABPIS. The polarization state of the incident proton beam was flipped (at 10 Hz) between two polarization states: the ''+'' state along the proton spin quantization axis, and the ''−'' state in the opposite direction. The spin quantization axis was aligned perpendicular to the reaction plane using a Wien filter. The Madison convention [26] defines the positive y axis as $\hat{k}_{\mathrm{in}}\times\hat{k}_{\mathrm{out}}$, where $\hat{k}_{\mathrm{in}}$ is the direction of the incident proton beam and $\hat{k}_{\mathrm{out}}$ is the direction of the outgoing γ ray. For the case of a detector on the left side of the beam line, the spin quantization axis corresponds to the $+y$ direction. Based on the formalism presented in [28], the vector analyzing power may be defined as

$$A_y(\theta,E)=\frac{Y^+(\theta,E)-Y^-(\theta,E)}{|p_y^+|Y^-(\theta,E)+|p_y^-|Y^+(\theta,E)}, \tag{6}$$

where Y^+ and Y^- denote the γ-ray yields for the ''+'' and ''−'' states, respectively, and p_y^+ and p_y^- denote the percent polarizations of the proton spin states. Polarizations of 70% were typically obtained. The values of p_y^+ and p_y^- were measured using a $^{12}\mathrm{C}(p,p)^{12}\mathrm{C}$ polarimeter at $E_p=6.18$ MeV [27].

The primary advantage associated with measuring the vector analyzing power is that it depends only on the ratio of yields, not on the absolute magnitude of the yields themselves. This means that the extraction of the energy dependence of A_y, unlike the cross section, does not require any knowledge of the stopping powers. The flipping of the spin state every tenth of a second ensured similar experimental conditions for each spin state. As a result, A_y can be expected to be independent of the systematic errors which are often present in cross section measurements.

J. Tensor analyzing power T_{20}

The measurement of the $^1\mathrm{H}(\vec{d},\gamma)^3\mathrm{He}$ tensor analyzing power $T_{20}(\theta)$ was performed with a tensor polarized deuteron beam from the ABPIS. The beam was fast spin-flipped between two spin states having different magnetic substate populations. We use the formalism of the Madison Convention [26] to describe these differing states in terms of the polarization p_{zz}. The states used were the ''+'' state, with (theoretical maximum) $p_{zz}^+=+1$, and the ''−'' state, with $p_{zz}^-=-1$. The quantization axis for both states was aligned with a Wien filter to be along the $\hat{k}_{\mathrm{in}}$ direction (and thus differs from the previous section). Typical values for $p_{zz}^{\pm}$ were ± 0.87. Based on the formalism presented in Ref. [28], the tensor analyzing power T_{20} can be defined as

$$T_{20}(\theta)=\sqrt{2}\frac{Y^+(\theta)-Y^-(\theta)}{|p_{zz}^+|Y^-(\theta)+|p_{zz}^-|Y^+(\theta)}, \tag{7}$$

where Y^- is the γ-ray yield associated with the ''−'' spin state, and Y^+ is associated with the ''+'' spin state.

The tensor analyzing power T_{20} is independent of the absolute magnitude of the yields for a given spin state. This fact, coupled with the fast spin-flip technique employed for the $(\vec{d},\gamma)$ study, makes this observable, as with A_y, independent of many systematic errors.

K. γ-ray polarization measurement

The γ-ray polarization $P_\gamma(\theta)$ for the $^2\mathrm{H}(p,\gamma)^3\mathrm{He}$ reaction was measured previously by Wilkinson [14] at an energy $E_p=1.1$ MeV. He found that the capture γ rays were completely plane polarized at 90° with respect to the beam axis $[P_\gamma(90°)=1]$, which is consistent with pure electric dipole radiation. In the current experiment, $P_\gamma(\theta)$ was measured in the energy region $E_p=80-0$ keV. The γ-ray polarization in this regime would be expected to be different from Wilkinson's measurement in the sense that the radiation is no longer pure electric dipole in nature, but now has a significant contribution from magnetic dipole transitions. Therefore, a measured $P_\gamma(\theta)$ of less than one would now be expected at these energies.

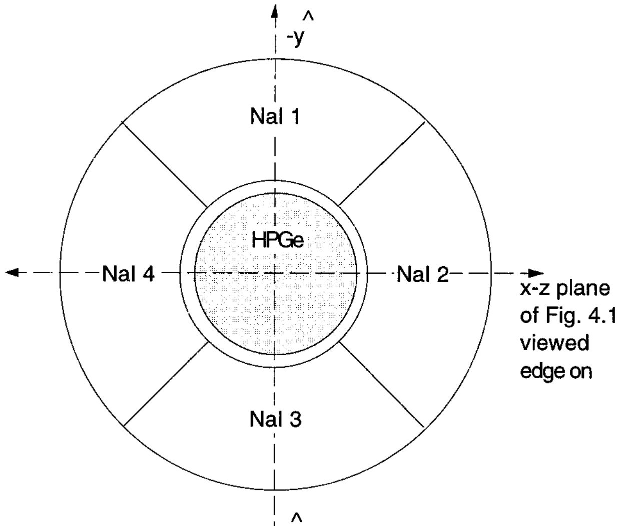

FIG. 7. A view of the HPGe and quadrated NaI(Tl) annulus as seen from the front. The horizontal line is the reaction plane viewed edge on. Linearly polarized γ rays hitting the HPGe will result in an up-down left-right asymmetry in the Compton scattering.

The technique used to measure the γ-ray polarization in the current experiment was to operate the quadrated NaI(Tl) annulus, which surrounded the HPGe detector, as a Compton polarimeter. Figure 7 shows the HPGe and NaI(Tl) annulus from a front view (the capture γ rays are incident into the page). Since γ rays are Compton scattered preferentially in a direction perpendicular to their electric vectors (as predicted by the Klein-Nishina formula), it is possible to determine the γ-ray polarization by measuring a left-right up-down asymmetry in the NaI(Tl) segments. In particular, $P_{\gamma}(\theta)$ is determined in terms of this measured asymmetry, $A(\theta)$, as follows:

$$P_{\gamma}(\theta)=\frac{A(\theta)}{S}, \tag{8}$$

where S is the polarization sensitivity of the Compton polarimeter at 5.5 MeV. The polarization sensitivity is a quantity which depends upon both detector geometry and energy thresholds used, and its measurement will be discussed in the next section. Looking at Fig. 7, if we define N_V to be the number of detected Compton-scattered events in detectors 1 and 3, and N_H to be the number of detected Compton-scattered events in detectors 2 and 4, the measured asymmetry $A(\theta)$ (for a given HPGe detector angle θ) is

$$A(\theta)=\frac{N_V-N_H}{N_V+N_H}. \tag{9}$$

The quantities N_V and N_H were measured by looking at events in the individual NaI(Tl) segments which were in coincidence with an event in the HPGe. To reduce the background coincidences [produced primarily by Compton scattered γ rays from sources other than ^{2}H$(p,\gamma)^{3}$He], a summed energy criteria was applied between the HPGe and NaI(Tl) signals whereby the total energy was required to sum to 5.5 MeV. Since a 5.5 MeV γ ray cannot deposit more than 5.26 MeV in the HPGe in a single scattering (via energy and momentum conservation), the threshold in the NaI(Tl) was set at 240 keV. Once implemented, the summed energy criteria eliminated coincident contributions from background sources like potassium-40 (1.46 MeV) and radiothorium (2.62 MeV). In order to eliminate any possible counting asymmetries caused by differences in the four NaI(Tl) segments, the annulus was periodically rotated by 90° after a set number of runs. The final quoted asymmetries were calculated by taking N_V and N_H to be a weighted average of the yields acquired from each of the four segments when rotated to the appropriate position.

L. Measurement of the γ-ray polarization sensitivity, S

In order to measure the ^{2}H$(p,\gamma)^{3}$He γ-ray linear polarization $P_{\gamma}(\theta)$ it was necessary to determine the polarization sensitivity, S, for the Compton polarimeter at $E_{\gamma}=5.5$ MeV. The technique used to obtain S at this energy was to actually measure its value at somewhat lower energies and then extrapolate the value upwards to 5.5 MeV. The value of S was actually measured at the energies of $E_{\gamma}=1.78$ and 4.43 MeV where it is possible to obtain γ rays of known polarization from other nuclear reactions. In particular, the ^{28}Si$(p,p'\gamma)^{28}$Si reaction at $E_p=3.1$ MeV [29] was used to obtain a γ ray of $E_{\gamma}=1.78$ MeV and the ^{12}C$(p,p'\gamma)^{12}$C reaction at $E_p=5.37$ MeV [29] was used to obtain a γ ray at $E_{\gamma}=4.43$ MeV.

Rather than rely on previous measurements of the γ-ray polarization for these reactions, we independently determined the γ-ray polarization at $\theta_{\rm lab}=90°$ by performing detailed measurements of the angular distributions. As discussed in Ref. [30], the polarization at 90°, for pure $E2$ radiation, is related to the reduced Legendre coefficients $a_2=A_2/A_0$ and $a_4=A_4/A_0$ as follows:

$$P_{\gamma}(90°)=\frac{(3/2)a_2+(5/8)a_4}{1-(1/2)a_2+(3/8)a_4}. \tag{10}$$

The angular distributions that we measured for the ^{28}Si$(p,p'\gamma)^{28}$Si and ^{12}C$(p,p'\gamma)^{12}$C reactions are shown in Fig. 8. The solid lines are Legendre fits to the data. The extracted coefficients are shown in Table I, along with the resulting polarizations as calculated using Eq. (10) [with systematic error included in the error bars for $P_{\gamma}(90°)$]. Table I also shows the experimental asymmetries which were measured with these γ rays at a laboratory angle of 90°. The polarization sensitivity for the energy in question was then calculated using Eq. (8), and the result is shown in the last row of Table I.

An energy dependence for the polarization sensitivity function can be obtained from the Klein-Nishina formula in the point-detector approximation, and is given by [16]

$$S(E_{\gamma})=\frac{C}{E_{\gamma}/0.511+0.511/(0.511+E_{\gamma})}, \tag{11}$$

where C is a normalization constant and E_{γ} is in MeV. Fitting the form of Eq. (11) to the measured polarization sensitivity data points (by minimizing the χ^2) yielded a value of $C=0.365\pm0.019$.

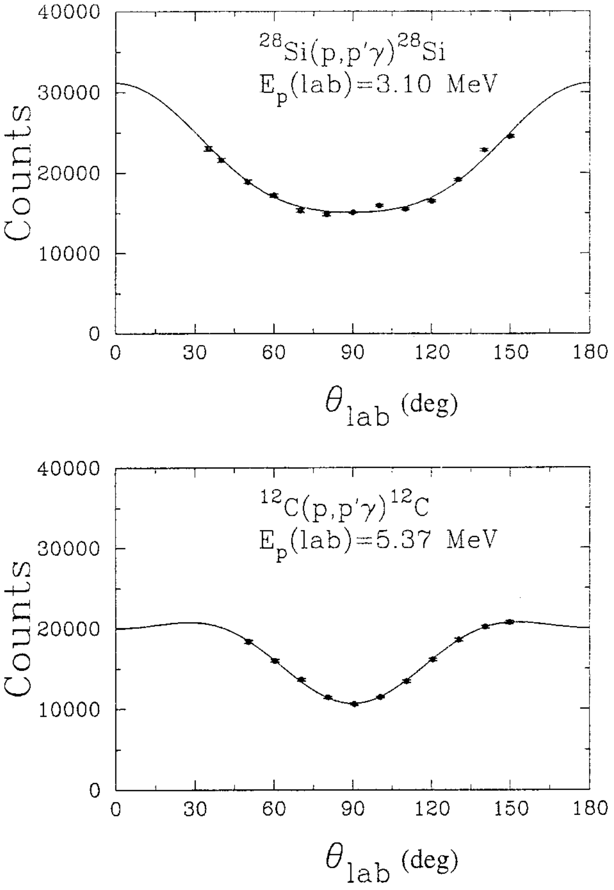

FIG. 8. The angular distributions measured for the ^{28}Si$(p,p'\gamma)$ and ^{12}C$(p,p'\gamma)$ reactions at $E_p = 3.1$ and 5.37 MeV, respectively. The solid lines are Legendre polynomial fits using the even coefficients. These fits were used to deduce the expected γ-ray polarization at 90°.

Figure 9 shows the polarization sensitivity data along with the fitted curve. The goodness of the fit indicates a correct assumption for the form of Eq. (11). From this curve, the extracted S value at 5.5 MeV is $S(5.5\ \text{MeV}) = 0.034 \pm 0.0034$, where systematic error is included in the error bar. The low polarization sensitivity of the current setup results from the large geometry of the NaI(Tl) annulus quadrants which, being far from the ideal point geometry case, tend to wash out the desired sensitivity.

III. DATA ANALYSIS

A. Raw HPGe spectra

Figure 10(a) shows the full response of the HPGe detector to 5.5 MeV incident γ rays. This spectrum was acquired at $\theta_{\text{lab}} = 90°$ over the course of approximately 5 days. Other spectra such as this were acquired at seven other angles (using both polarized and unpolarized beams). To better show the details of the full response, the spectrum, shown in Fig. 10(a), was not subject to anticoincidence with the NaI(Tl) shield. The large peak at 5.5 MeV represents full energy absorption, while the peaks at 5.0 and 4.5 MeV are the first and second escape peaks, respectively. The shallow bumps between these peaks represent Compton scattering.

TABLE I. Results of the polarization sensitivity measurement.

	^{28}Si$(p,p'\gamma)$	^{12}C$(p,p'\gamma)$
E_γ	1.78 MeV	4.43 MeV
a_2	0.513 ± 0.008	0.492 ± 0.013
a_4	0.138 ± 0.011	-0.239 ± 0.015
$P_\gamma(90)$	1.07 ± 0.08	0.88 ± 0.04
$A(90)$	0.107 ± 0.002	0.036 ± 0.002
$S(E_\gamma)$	0.100 ± 0.008	0.041 ± 0.003

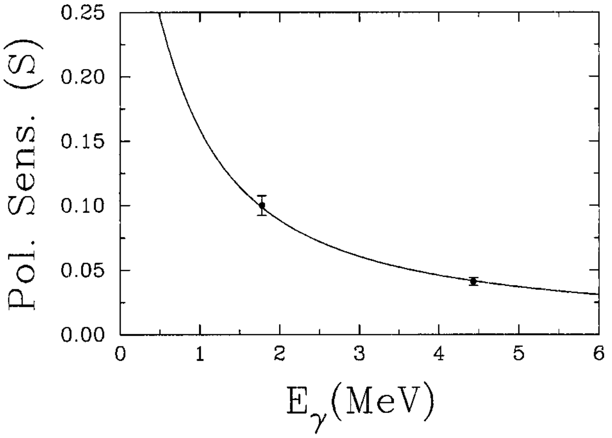

FIG. 9. The polarization sensitivity of the current HPGe-NaI(Tl) setup when operated as a Compton polarimeter. The two points at 1.78 and 4.43 MeV were measured using the γ rays from the ^{28}Si$(p,p'\gamma)$ and ^{12}C$(p,p'\gamma)$ reactions. The solid line is a fit using the formula for point-detector geometry.

Figure 10(b) shows an expanded view of the full energy peak shown in Fig. 10(a). To show the reduction in back-

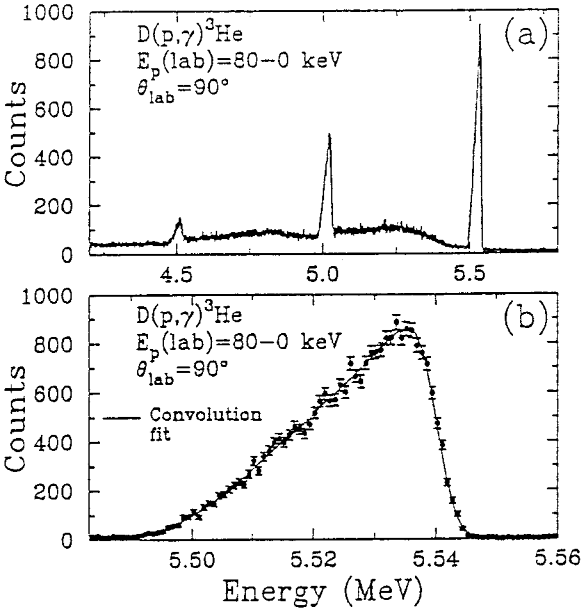

FIG. 10. A HPGe spectrum for ^{2}H$(p,\gamma)^3$He taken at a lab angle of 90°. The full detector response [not anticoincidenced with the NaI(Tl) annulus] is shown in (a), while the spectrum in (b) is a blowup of the full energy peak (with the anticoincidence condition applied).

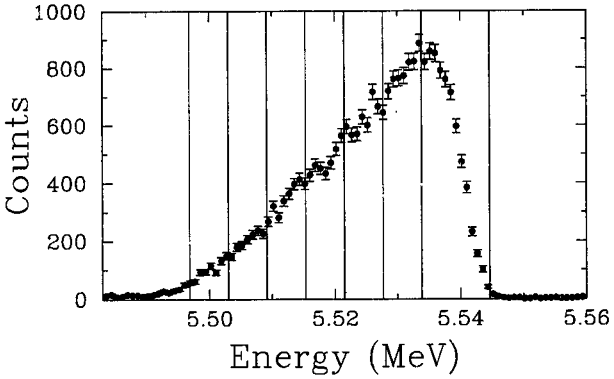

FIG. 11. The full energy peak of Fig. 10(b) showing the location of the seven energy bins.

ground that can be achieved, Fig. 10(b) shows the HPGe spectrum in anticoincidence with the NaI(Tl) shield. Although the intrinsic resolution of the HPGe at 5.5 MeV is 4.2 keV, the peak in Fig. 10(b) is seen to be about 50 keV wide. This width arises due to the fact that we are stopping an 80 keV proton beam in the target, and thus the range of incident proton energies produces a range of outgoing γ-ray energies.

B. The binning analysis

Since the intrinsic resolution of the HPGe at 5.5 MeV is 4.2 keV (see Sec. III C), a simple binning of the full energy peak would seem an appropriate technique for obtaining the energy dependence of the ^{2}H(p,γ)^{3}He cross section. Figure 11 shows the full energy peak binned into regions of equal laboratory beam energies. The first bin encompasses the region $E_p = 10$–20 keV, and the second $E_p = 20$–30 keV, and so on up to $E_p = 70$–80 keV. These seven bins are henceforth identified by their center-of-bin beam energy, $\overline{E_p}$ (i.e., the top bin has $\overline{E_p} = 75$ keV). The energy calibration of this spectrum is obtained as follows: known background peaks which are present in the HPGe spectrum (potassium-40 and radiothorium) gave the keV per channel to within 0.5% (at 5.5 MeV), while the absolute energy scale was determined by knowing that the middle of the slope of the right-hand side of the ^{2}H(p,γ)^{3}He full energy peak was equal to 5.54 MeV (the γ-ray energy corresponding to the highest proton energy). Using this technique, we estimate that the energy scale in the vicinity of 5.5 MeV was accurate to within ± 1 keV.

By acquiring γ-ray yields for the seven bins in question (using both polarized and unpolarized beams), the $\sigma(\theta)$, $S(\theta)$, and $A_y(\theta)$ observables could be calculated for each energy region. In order to calculate the cross section for a given bin, it was also necessary to integrate the deuterium areal density over the range of energies present (e.g., for the top bin, the deuterium areal density was 8×10^{17} deuterons/cm^2). Cosmic background radiation was accounted for by monitoring an energy window just above the full energy peak, and then subtracting out the appropriate number of counts/channel.

Another background component considered was the long, low energy tail associated with the response function of the full energy peak. For our thick target yield, tails from the full range of beam energies combine to produce an energy dependent background. To account for this the HPGe intrinsic response function was modeled (see Sec. III C) and the effects of the low energy tailing were subtracted from each bin (details appear in Ref. [16]). The effects of the primary part of the HPGe intrinsic response function were neglected in the binning analysis since it was assumed that the Gaussian intrinsic response acted simply like a smoothing function on the raw spectra. The one exception to this rule was the top bin, where the size of the bin was widened in order to encompass the ^{2}H(p,γ)^{3}He strength ‘‘folded out’’ by the response function. This type of ‘‘edge effect’’ should not be present for any of the other bins.

C. The deconvolution analysis

The goal of the deconvolution analysis was to remove the effect of the HPGe detector response and the effects of the changing deuterium areal density from the raw spectra in order to view directly the energy dependence of the ^{2}H(p,γ)^{3}He S factor. The method used to perform this ‘‘deconvolution’’ of the raw spectra was that of a convolution fit. The steps of this procedure were as follows.

(1) Derive a functional form for the energy dependence of the ^{2}H(p,γ)^{3}He yield in terms of the deuterium areal density and a parameterized form of the S factor.

(2) Derive a functional form for the HPGe response function at $E_\gamma = 5.5$ MeV.

(3) Convolute the yield function and HPGe response function together, and then fit the resulting curve directly to the raw spectra. This will determine the parameters in the yield function, and will give us a functional form for the ^{2}H(p,γ)^{3}He S factor.

The first step of this procedure used Eqs. (5) and (3) to define the ^{2}H(p,γ)^{3}He yield in terms of the cross section, and then used Eq. (1) to express the cross section in terms of the S factor. In order to parametrize this function, a linear energy dependence was assumed for the differential S factor: $S(\theta,E_{\text{c.m.}}) = S_0(\theta) + S_1(\theta)E_{\text{c.m.}}$. This form is a reasonable assumption based on the results of many low energy capture experiments [10]. Using the linear S-factor assumption, we obtain the following form for the differential ^{2}H(p,γ)^{3}He yield:

$$Y(\theta,E_p) = \frac{S_0(\theta) + E_{\text{c.m.}} S_1(\theta)}{E_{\text{c.m.}}} e^{-2\pi\eta}[D(E_p)](P)(\epsilon d\Omega), \tag{12}$$

where $E_{\text{c.m.}} = (2/3)E_p$, and $S_0(\theta)$ and $S_1(\theta)$ are the parameters to be determined.

The second step of the deconvolution procedure was to derive a functional form for the total HPGe response function. The total HPGe response function is actually a convolution of two component response functions: an intrinsic response function due to the interaction of a monoenergetic γ ray with the HPGe crystal; and a so-called ‘‘kinematic’’ response function which arises as a result of the finite geometry of the experimental setup (γ rays emitted at different angles have different energies). The intrinsic full energy peak response function of the HPGe was studied using a ^{66}Ga source [created in the lab by means of the ^{63}Cu(α,n)^{66}Ga reaction at $E_\alpha = 18$ MeV]. By means of the

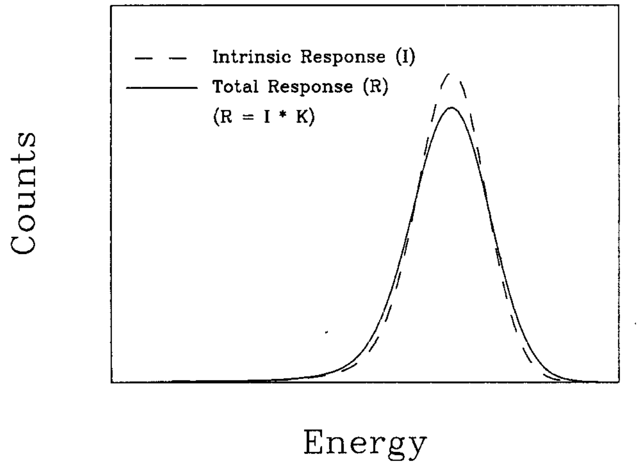

FIG. 12. The intrinsic response of the HPGe detector at 5.5 MeV, as obtained by measuring γ rays from the ^{66}Ga decay, is shown by the dashed line. The solid line represents the convolution of this intrinsic response function with the calculated kinematic response function (as derived, in this case, for $E_p = 80$ keV).

^{66}Ga($\beta^+ +$EC)^{66}Zn decay, excited states in ^{66}Zn are populated, and these states γ decay producing γ rays ranging from 0.83 to 4.81 MeV. To determine the energy dependence of the intrinsic monoenergetic response function, measured peaks from this source were fit to a parametrized form composed of the following components: a primary Gaussian, a skewed Gaussian, and a smoothed step function (which is the low energy "tail" previously mentioned). The extracted parameters were then extrapolated to 5.5 MeV.

The kinematic response function was obtained by means of a Monte Carlo simulation (the EGS4 code from Stanford [31]). By simulating the target-detector geometry of the actual experiment, γ rays were launched isotropically from a point source, and the θ dependence of the response function was noted. The "kinematic" response function was created by transforming this θ dependence into an E_γ dependence using kinematic relationships. Figure 12 shows, by the dashed line, the normalized intrinsic response function of the HPGe at 5.5 MeV. The solid line represents the total HPGe response function, which is a convolution of the intrinsic and kinematic parts. We conclude from this figure that the intrinsic response function dominates the total response.

The final step of the deconvolution procedure is to convolute the total HPGe response function and the parametrized yield function, and then fit this composite function directly to the raw spectra. The processor used to fit the spectra was the MINUIT χ^2 minimization package [32]. Figure 10(b) shows the full energy peak along with a convolution fit (solid line). The fit is excellent, and has a χ^2/ν of 1.0. The $S_0(\theta)$ and $S_1(\theta)$ parameters and the differential S factor $S(E_{\mathrm{c.m.}},\theta)$ were determined by performing fits like this to the spectra at every angle θ. The total angle integrated S factor is then

$$S(E_{\mathrm{c.m.}}) = \int S_0(\theta)\,d\Omega + E_{\mathrm{c.m.}}\int S_1(\theta)\,d\Omega = S_0' + E_{\mathrm{c.m.}}S_1'. \tag{13}$$

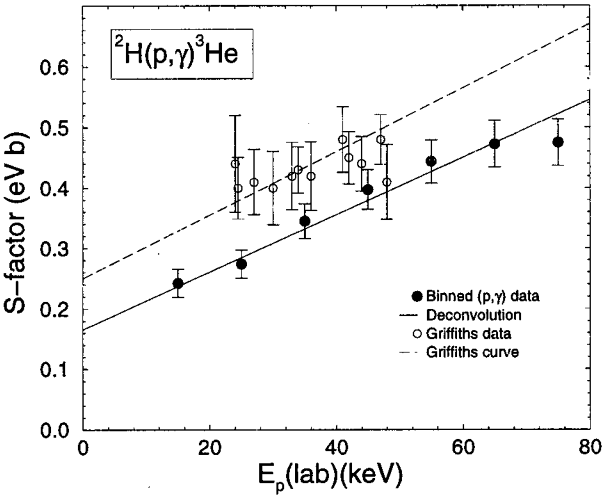

FIG. 13. The current S-factor results, as shown by the solid data points (binned data) and solid line (deconvolution analysis), are compared with the previous results of Griffiths *et al.*, as shown by the open data points and dashed line. A systematic error of 9% is included in each of the solid data points to indicate the total uncertainty of the measurements.

In Fig. 13, the deconvolution result for the total ^{2}H$(p,\gamma)^3$He S factor is shown by the solid line, where $S(E_{\mathrm{c.m.}}) = S_0 + E_{\mathrm{c.m.}}S_1$. The parameters for this curve are $S_0 = 0.166 \pm 0.005$ eV b and $S_1 = 0.0071 \pm 0.0004$ eV b keV^{-1}, where the quoted errors are statistical only. The solid data points are the results from the binning analysis based on $\sigma_T = 4\pi A_0$, with A_0 from the Legendre fit procedure. The systematic error of 9% (see Sec. II H) is included in these data points in order to show the total uncertainty involved. The solid line and data points agree well with each other. Note that these data points and curve are equivalent to those presented in Refs. [2,3] but not in Ref. [1], where an efficiency error caused an overall shift (see discussion in Refs. [2,3]). The open data points and dashed line are the previous results of Ref. [12].

The difference in absolute scale between the data points of Ref. [12] and the current data points is due primarily to the different stopping powers used (as discussed in Sec. II F). Furthermore, as is clear from the figure, the current data unambiguously define a slope for the S factor. Based on the solid line, the currently extracted S factor at zero energy is 0.166 ± 0.014 eV b, which is about 35% lower than the value derived by the Griffiths extrapolation (via the dashed line, which is a direct capture calculation normalized to their data). Furthermore, the energy dependence currently extracted via the solid line is somewhat different than the energy dependence predicted by the direct capture calculation of Griffiths *et al.* For example, if the calculation of Griffiths *et al.* is normalized to the current data point at $\overline{E}_p = 45$ keV, the result is a linear S-factor curve with parameters $S_0 = 0.21$ and $S_1 = 0.0065$. Clearly, the $S(0)$ value derived in this manner overpredicts the currently extracted value by approximately 25%.

Figure 14 shows the vector analyzing power at $\theta_{\mathrm{lab}} = 90°$ as a function of energy. The solid line is the deconvolution result while the data points are from the binning analy-

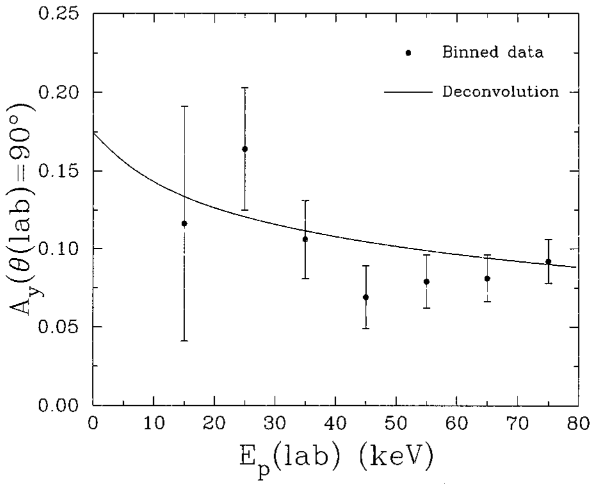

FIG. 14. The vector analyzing power at 90° as a function of incident beam energy. The solid points are the results of the binning analysis, while the solid line is the result of the deconvolution analysis.

sis. The increasing importance of $M1$ radiation at low energies is apparent here.

D. Legendre fit

A fit to Legendre and associated Legendre polynomials was performed on the acquired $\sigma(\theta)$ and $A_y(\theta)$ binned data at each energy. The $T_{20}(\theta)$, obtained from the ^{1}H($\vec{d},\gamma$)^{3}He reaction measurements, were not binned, but were fitted using the entire energy averaged data set. In particular, the data were fit as follows:

$$\begin{aligned}\sigma(\theta)&=\sum_{k=0}^{n} Q_k A_k P_k(\cos\theta),\\ \sigma(\theta)A_y(\theta)&=\sum_{k=1}^{n} Q_k B_k P_k^1(\cos\theta),\\ \sigma(\theta)T_{20}(\theta)&=\sum_{k=0}^{n} Q_k C_k P_k(\cos\theta),\end{aligned} \tag{14}$$

where the Q_k are the finite geometry correction coefficients [33], P_k and P_k^1 are the Legendre and first associated Legendre polynomials, respectively, and the A_k, B_k, and C_k coefficients are the parameters which were obtained from the fit to the data. It was found that satisfactory fits could be obtained in all cases if $n=2$. The normalized coefficients [$a_k=A_k/A_0$, $b_k=B_k/A_0$, and (for the unbinned T_{20} data) $c_k=C_k/A_0$] are listed in Table II.

E. Transition-matrix element analysis

The $\sigma(\theta)$ and $A_y(\theta)$ binned data were also subjected to a transition matrix element (TME) analysis. Although analyses were attempted which used the four $E1$ and $M1$ matrix elements listed in Fig. 1, the resulting seven free parameters (four amplitudes and three relative phases) yielded multiple solutions. To determine a unique solution both the two $E1$ matrix elements and the two $M1$ matrix elements were constrained to have equal amplitudes and phases. The $E1$ constraint is equivalent to assuming a pure $\sin^2\theta$ form for the $E1$ angular distribution, while the $M1$ assumption is justified on the basis of lack of sensitivity to $s=1/2$ vs $s=3/2$ $M1$ strength in the structure of the equations for $\sigma(\theta)$ and $A_y(\theta)$. These constraints reduced the analysis to three free parameters: an s-wave $M1$ amplitude (S); a p-wave $E1$ amplitude (P), and a relative phase (Δ). Using the formalism given in Ref. [28], the Legendre coefficients described above can be expanded in terms of S, P, and Δ as follows:

$$\begin{aligned}A_0&=6P^2+6S^2,\\ A_1&=0,\\ A_2&=-6P^2,\\ B_1&=-10(P)(S)\sin\Delta,\\ B_2&=0.\end{aligned} \tag{15}$$

In this manner an $E1$ amplitude, an $M1$ amplitude, and a relative phase were extracted for each set of binned data. Note that the B_1 coefficient is dependent upon $E1$-$M1$ interference for its existence, and thus demonstrates the potential power of the $A_y(\theta)$ observable in determining the $M1$ fraction of the total cross section. The total cross section can be defined in terms of these parameters by $\sigma_T=4\pi A_0=24\pi(P^2+S^2)$. In addition, the $M1$ fraction of the total cross section (the "$M1$%") can be determined as follows:

TABLE II. Results of the Legendre polynomial fit. Coefficients for the fits to the cross section (A_0, a_1, and a_2) and vector analyzing power (b_1) are presented for each of seven 10 keV wide energy bins. The c_k coefficients are for the energy-integrated data (E_d=80-0 keV).

Coeff.	15 keV	25 keV	35 keV	45 keV	55 keV	65 keV	75 keV
A_0 (nb)	0.581±0.030	2.45±0.067	5.83±0.11	9.77±0.15	14.0±0.18	17.7±0.27	20.1±0.27
a_1	0.027±0.120	0.063±0.063	−0.12±0.04	−0.11±0.04	−0.10±0.03	−0.055±0.027	0.024±0.026
a_2	−0.560±0.112	−0.72±0.06	−0.60±0.04	−0.67±0.03	−0.69±0.03	−0.77±0.03	−0.86±0.02
b_1	0.185±0.081	0.223±0.043	0.122±0.027	0.107±0.022	0.115±0.018	0.11±0.02	0.13±0.02
c_0				−0.066±0.013			
c_1				−0.078±0.014			
c_2				0.262±0.027			

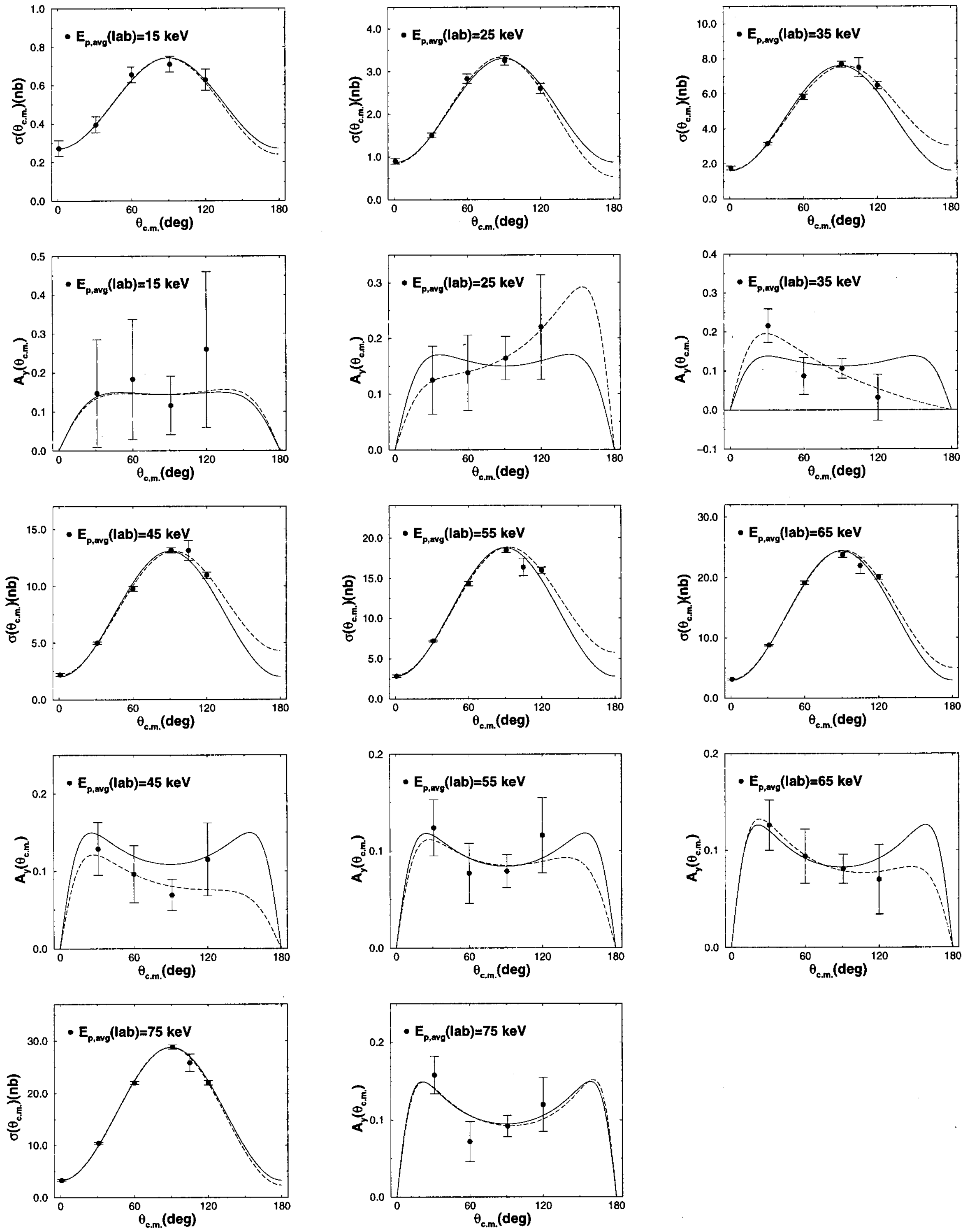

FIG. 15. The binned ^{2}H($\vec{p},\gamma$)^{3}He data at E_p=15,25,35,45,55,65,75 keV. The dashed line is a Legendre fit while the solid line is a simultaneous TME fit to both observables [see Eq. (15)].

$$M1\% = \frac{S^2}{S^2+P^2}\times 100. \tag{16}$$

Figure 15 shows the $\sigma(\theta)$ and $A_y(\theta)$ data acquired from the binning analysis. The results of a Legendre fit to the data (dashed line) and a transition matrix element analysis (solid line) are shown along with the binned data. Examining the results from the seven bins, we notice that the angular distri-

TABLE III. Amplitudes and relative phases from the TME analysis.

	15 keV	25 keV	35 keV	45 keV	55 keV	65 keV	75 keV
ν	6	6	7	7	7	7	7
χ^2/ν	0.27	0.55	2.21	2.19	2.94	1.47	1.77
P	0.196 ± 0.010	0.445 ± 0.010	0.700 ± 0.010	0.947 ± 0.010	1.14 ± 0.01	1.32 ± 0.01	1.44 ± 0.01
S	0.182 ± 0.010	0.325 ± 0.010	0.440 ± 0.011	0.499 ± 0.012	0.584 ± 0.013	0.602 ± 0.013	0.632 ± 0.014
Δ	12.7 ± 5.2	14.5 ± 2.7	11.7 ± 1.9	9.7 ± 1.6	10.0 ± 1.4	10.7 ± 1.33	12.7 ± 1.29
%$M1$	46.5 ± 3.6	34.7 ± 1.6	28.3 ± 1.1	21.7 ± 0.8	20.8 ± 0.7	17.2 ± 0.6	16.2 ± 0.5

butions become more isotropic as we go lower in energy. Since we expect the p-wave $E1$ to have a $\sin^2\theta$ distribution and the s-wave $M1$ to have an isotropic distribution, we interpret this trend toward isotropy as indicating the increasing presence of $M1$ at the lower energies. We also notice from Fig. 15 that the transition matrix element fit does a fairly good job of representing the angular distribution over all energies measured. This indicates that the assumptions we made in the TME analysis were reasonable. Furthermore, this validates the analysis done by Griffiths *et al.* [12], who assumed $\sigma(\theta)=C_1\sin^2\theta+C_2$, where C_1 and C_2 are constants. This is the first time that this shape has been experimentally verified to a high degree of accuracy at these low energies.

The extracted Legendre coefficients as a function of bin energy in terms of $a_1=A_1/A_0$ and $a_2=A_2/A_0$, were presented in Table. II. The A_0 coefficient, being proportional to the total cross section, falls rapidly due primarily to the Coulomb barrier. The a_1 coefficient, representing the asymmetry in the angular distribution, is essentially consistent with zero. The b_1 coefficient, which by Eq. (15) arises from $E1$-$M1$ mixing, rises with decreasing energy and, as seen previously in Fig. 14, indicates that an increasing amount of M1 is present as the energy decreases. The b_2 coefficient is consistent with zero.

Table III shows the numerical results of the TME analysis for the binned ^{2}H(p,γ)^{3}He, with separate rows for the number of degrees of freedom (ν), the chi-squared per degree of freedom (χ^2/ν), the p-wave $E1$ amplitude (P), the s-wave $M1$ amplitude (S), the relative phase (Δ), and the $M1$ fraction of the total ^{2}H(p,γ)^{3}He cross section (%$M1$). The $M1$ fraction is plotted in Fig. 16 where we see that the %$M1$ clearly rises as the beam energy lowers, approaching 50% at the lowest energies.

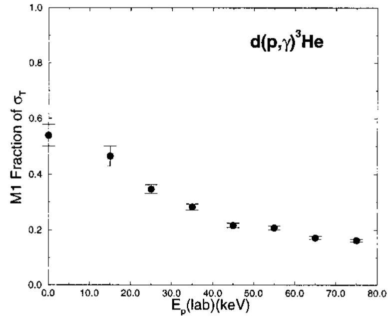

FIG. 16. The $M1$ fraction of σ_T vs beam energy as extracted from the TME analysis of the binned data.

The deconvolution analysis performed separately for the data at each angle provided angular distributions of the cross section [or, equivalently, the S factor: $S(\theta)$] and analyzing powers at zero energy. The results are shown in Fig. 17 along with the TME [using Eqs. (15)] and Legendre polynomial (see Sec. III D) fits to these data. The resulting TME amplitudes and phases, as well as the Legendre polynomial coefficients are presented in Table IV (see also Fig. 17). The TME analysis indicates that 54% of the cross section at $E=0$ keV arises from $M1$ radiative s-wave capture. These results can also be used to determine the S factor at $E=0$ due to $M1(S_s)$ and $E1(S_p)$ radiation separately. The results are $S_s(E=0)=0.109\pm0.010$ eV b and $S_p(E=0)=0.073\pm0.007$ eV b, respectively.

A second TME analysis was performed simultaneously on the results (see Fig. 18) of all four polarization observables for $E_{\text{c.m.}}<27$ keV. Unfortunately, the statistics acquired for the T_{20} data were limited and prevented us from obtaining the energy dependence of this observable. As a result, the fit was performed with respect to integrated yields over the center-of-mass energy range from 0 to 27 keV. In particular, the fit was performed on cross section data from both the ^{1}H(d,γ)^{3}He and ^{2}H(p,γ)^{3}He reactions, vector analyzing power data from the ^{2}H($\vec{p},\gamma$)^{3}He reaction, tensor analyzing power T_{20} data from the ^{1}H($\vec{d},\gamma$)^{3}He reaction, and γ-ray polarization data from the ^{2}H(p,γ)^{3}He reaction.

In order to combine the cross section data sets from both the ^{2}H(p,γ)^{3}He and ^{1}H(d,γ)^{3}He reactions, the (p,γ) for $E_p=40-0$ keV, corresponding to $E_{\text{c.m.}}=27-0$ keV and $E_d=80-0$ keV, were extracted from the full (p,γ) data set. The cross section data for the ^{1}H(d,γ)^{3}He reaction at $E_{\text{c.m.}}<27$ keV were then transformed using $\theta_p\rightarrow180-\theta_d$ and treated as back angle data from the perspective of the ^{2}H(p,γ)^{3}He reaction. We also note that, due to insufficient statistics, the P_γ data used in the fit were an integrated yield over the center-of-mass energy range 0–54 keV.

In this second fitting procedure six TME's were used, including the four $E1$ and $M1$ terms described in Fig. 1 and the two $E1$ terms with $s=3/2$, $j=1/2,3/2$. These terms were previously omitted since the $\sigma(\theta)$ and $A_y(\theta)$ observables, unlike $T_{20}(\theta)$, are insensitive to them. We obtained T_{20} data that extend from 0° to 150°, and consequently were able to determine the fore-aft asymmetry of T_{20}. The Legendre coefficient which quantifies this asymmetry is the c_1 coefficient. This fore-aft asymmetry must arise from interference between radiations having opposite parity (in this case $E1$ and $M1$) and between terms whose s and s' triangulate to 2. Since the dominant $E1$ term has $s=1/2$, the $s=3/2$ $M1$ term will affect this asymmetry much more than the $s=1/2$ $M1$

TABLE IV. Results from the Legendre polynomial and TME fits to the zero-energy data of Fig. 17. The coefficients in this table include statistical error and errors from the deconvolution process.

a_1	a_2	b_1	b_2	
0.093 ± 0.077	-0.537 ± 0.081	0.251 ± 0.067	0.061 ± 0.040	
ν	χ^2/ν	% $E1$ strength	% $M1$ strength	$M1$-$E1$ phase (deg)
6	1.04	46.1 ± 3.8	53.9 ± 3.9	21.7 ± 3.6

term. This should therefore allow us to determine the relative strength of the two contributing $M1$ terms [$s=1/2$ (doublet) vs. $s=3/2$ (quartet)].

The best fit, shown in Fig. 18, had a $\chi^2/\nu=1.57$ and TME amplitudes whose values are given in Table V. The Legendre coefficients of this fit have been listed in Table II. The c_1 coefficient, which quantifies the fore-aft asymmetry in T_{20}, appears to be the most sensitive to the distribution of strength between the doublet and quartet $M1$ terms. The results of the analysis indicate that the ratio of the intensities for $s=3/2$ to $s=1/2$ is 1.35 ± 0.69. This result can be compared to the theoretical prediction of Friar *et al.* [4], which gives a value of 0.6, or to the recent result of Viviani *et al.* [34] at 80 k eV, which gives 0.5 when MEC effects (two-body currents) are included and 2.1 for the nucleons-only calculation. Although the present result appears to be in disagreement with theory, the error is too large to claim a serious discrepancy. It is important, however, to point out the sensitivity of this ratio to the detailed treatment of MEC's in the calculations. As stated earlier, the most directly determined experimental quantity which is sensitive to this is the c_1 coefficient obtained from the Legendre polynomial fit to the $T_{20}(\theta)$ data. The experimentally determined value of this coefficient obtained from this fit is $c_1=-0.078\pm0.014$, which disagrees with the theoretical value from Ref. [34] of $c_1=-0.0134$.

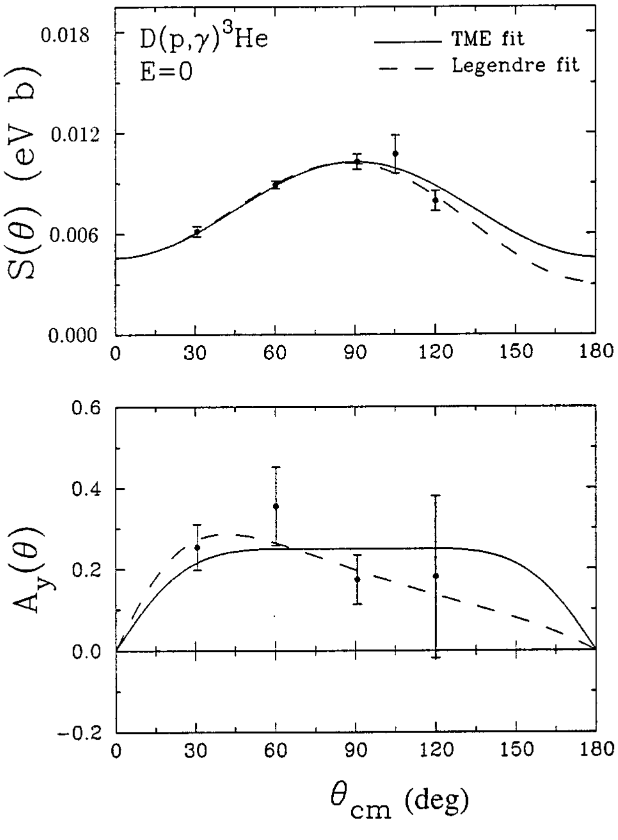

FIG. 17. The results of the deconvolution analysis at zero energy are presented here as data points. The solid line is a TME fit while the dashed line is a Legendre fit.

F. Determination of the asymptotic *D*- to *S*-state ratio

The exceptionally low center-of-mass energies involved in the present study of the $^1\mathrm{H}(\vec{d},\gamma)^3\mathrm{He}$ reaction provide an excellent opportunity to extract a value of the asymptotic D- to S-state ratio, η, for ^{3}He. This ratio describes the relative strength of the D-state and S-state components of the bound state wave function for ^{3}He. It has been shown [35] that the low energy tensor analyzing powers are sensitive to this ratio. However, an extraction of η by Vetterli *et al.* [36] from $^1\mathrm{H}(\vec{d},\gamma)^3\mathrm{He}$ at $E_d=19.8$ MeV found the result to be highly dependent on the choice of bound state wave functions. Specifically, Vetterli found that a significant portion of the reaction strength occurred in the region of p-d separation less than three fermis, showing that the approximation of the reaction taking place in the asymptotic region of the wave function to be marginal at best.

At the current $E_{\mathrm{c.m.}}\leqslant 27$ keV, however, the approximation that the reaction takes place in the asymptotic region of the

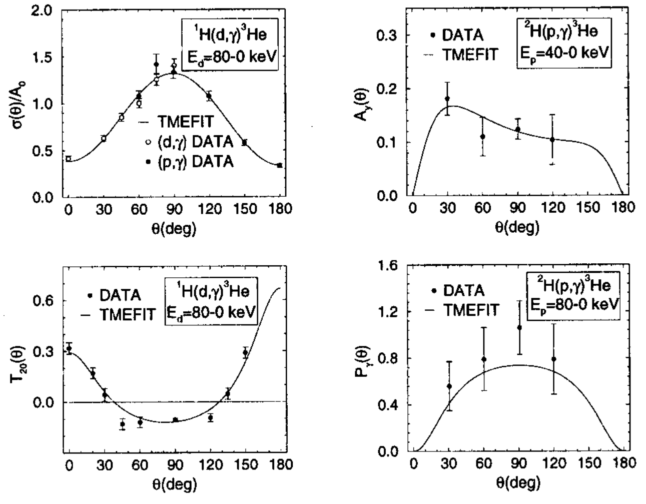

FIG. 18. Results of the simultaneous TME fit to all data with $E_{\mathrm{c.m.}}<27$ keV. The solid line is the fit, which has $\chi^2/\nu=1.57$.

TABLE V. TME amplitudes and phases for the constrained TME fit to data with $E_{c.m.}<27$ keV.

TME	Amplitude	Phase
$E1^2p_2$	0.571 ± 0.009	0.000 ± 0.000
$E1^2p_4$	0.571 ± 0.009	0.000 ± 0.000
$E1^4p_2$	0.231 ± 0.061	-100.9 ± 6.1
$E1^4p_4$	0.105 ± 0.035	92.0 ± 6.4
$M1^2s_2$	0.443 ± 0.088	-48.2 ± 8.82
$M1^4s_4$	0.363 ± 0.056	-9.0 ± 4.53

wave function does appear to be justified. Table VI shows the contribution to the total cross section in one fermi bins from direct capture calculations performed at $E_d=19.8$ MeV [37] and $E_d=80$ keV. These calculations were performed using realistic $p+d$ wave functions obtained by Gibson and Lehman [38] from a full three-body Faddeev calculation. The table clearly shows that at 80 keV ~ 93% of the reaction strength occurs beyond three fermis, compared with ~ 65% at 19.8 MeV.

The details of the extraction of η are given in Ref. [39]. In summary, however, ''matched'' bound state wave functions for the S and D components of ^{3}He were constructed from the asymptotic forms and the realistic wave functions from Lehman and Gibson described above. Direct capture calculations of $T_{20}(90°)$ were performed as a function of η, which is essentially the choice of the relative strength between the overall normalizations of the D- and S-state components of the bound state wave function. These results were then compared with the measured data for T_{20} to obtain a best-fit value for η of $-0.0399\pm0.0091^{+0.0012}_{-0.0019}$. The last error represents rough limits on the model dependence due to the choice of bound state wave functions inside of five fermis.

The results of the present measurement agree well with other recent experimental and theoretical determinations of η. Representative of recent experimental work, Ayer *et al.* [40], using a DWBA extraction of η from ($\vec{d}$,^{3}He) reactions, found $\eta=-0.0386\pm0.0046\pm0.0012$. On the theoretical side, Friar *et al.* [41] performed full three-body Faddeev calculations including Coulomb effects using diverse models for the two- and three-body NN forces and found $\eta=-0.0430\pm0.001$. The present measurement agrees within error with both these results (and others—see the summary in Ayer *et al.* [40]). Again, the interested reader is referred to Ref. [39] for a detailed discussion of this determination of η.

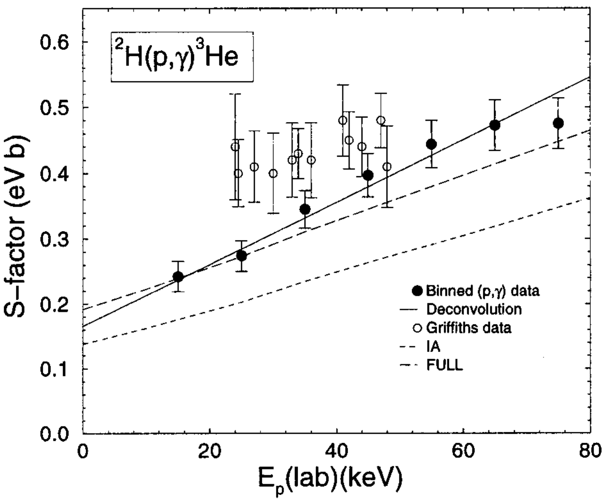

FIG. 19. The S-factor data of the current experiment (solid points and solid line) and previous experiment (open points) shown along with the results of a rigorous three-body calculation (dashed and dotted lines). The dashed line includes meson exchange currents, while the dotted line does not. A systematic error of 9% is included in each of the solid data points to indicate the total uncertainty of the measurements.

IV. SUMMARY OF RESULTS

The results of this study indicate a value for the S factor of the ^{2}H(p,γ)^{3}He at zero energy of $S=0.166\pm0.014$ eV b. The error given here includes both statistical and systematic components. This value was obtained assuming a linear energy dependence (justified on the basis of the excellent fit to the measured energy dependence) given by $S(E_{\text{c.m.}})=S_0+E_{\text{c.m.}}S_1$, with $E_{\text{c.m.}}$ in keV. The experimentally determined values were $S_0=0.166\pm0.005$ eV b and $S_1=0.0071\pm0.0004$ eV b keV^{-1}, where the errors are statistical only. The deconvolution fit, when extrapolated to zero energy energy, indicates that the percentage of $M1$ capture in the zero cross section is 54% ± 4%. This analysis also allows for a determination of the s-wave and p-wave parts of the total S-factor at zero energy. The results are $S_s(E=0)=0.109\pm0.010$ eV b and $S_p(E=0)=0.073\pm0.007$ eV b. The detailed results of the angular distribution measurements of both cross section and analyzing powers are best summarized in Tables II, III, IV, and V. Finally, the tensor analyzing power $T_{20}(\theta)$, when combined with all other data from this experiment, yield a value for the asymptotic D- to S-state ratio η for ^{3}He of $\eta=-0.0399\pm0.0091^{+0.0012}_{-0.0019}$.

V. CONCLUSIONS

A. Three body calculation

The comparison of the current data to recent three-body theory has been discussed in Ref. [2] and the details of the theoretical work have been presented in Ref. [34]. Figures 19

TABLE VI. Percentage of σ_{total} calculated as a function of p-d separation distance for realistic choice of ^{3}He wave function.

	p-d separation (fm)							
E_d (MeV)	0.1–1.0	1.0–2.0	2.0–3.0	3.0–4.0	4.0–5.0	5.0–6.0	6.0–7.0	7.0
19.8	0.7%	10.5%	23.7%	27.6%	21.4%	11.5%	3.9%	0.7%
0.080	0.0	2.2%	5.2%	10.4%	12.3%	13.6%	13.3%	43.0%

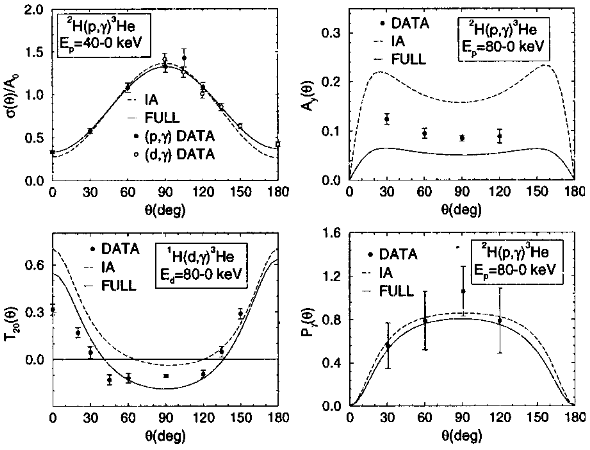

FIG. 20. A comparison between experimental values and results of variational calculations for $\sigma(\theta)$, $A_y(\theta)$, and $P_\gamma(\theta)$ for the ^{2}H$(p,\gamma)^3$He reaction, and $\sigma(\theta)$, $T_{20}(\theta)$ for the $p(d,\gamma)^3$He reaction. In each plot, the solid curve corresponds to the results obtained with one- and two-body currents while the dashed curve is obtained in the impulse approximation.

and 20 show the current S factor, $\sigma(\theta)$, $A_y(\theta)$, T_{20}, and $P_\gamma(\theta)$ data along with the recent three-body calculations discussed in Ref. [2]. The dotted line is a calculation that neglects meson exchange currents and Δ-isobar effects, while the dashed line is a calculation that includes them. The importance of explicitly including MEC's and Δ-isobar effects in the calculation is clearly demonstrated in the case of the S-factor data, where the agreement with the full theoretical calculation is seen to be fairly good. In the case of the current $A_y(\theta)$ and $T_{20}(\theta)$ data, the disagreement with theory is a subject of considerable interest, and investigations are underway. The fact that the theoretical results show strong sensitivities to the effects of meson-exchange currents in these polarization observables indicates this usefulness in testing the details of these calculations. The agreement of the current $P_\gamma(\theta)$ data and the results of the three-body theory are seen to be quite good. This, of course, must be viewed in the light of the large error bars on the current $P_\gamma(\theta)$ data.

B. Astrophysical consequences of current results

The protostellar evolution calculation of Ref. [11] used the results of Griffiths *et al.* (the dashed line in Fig. 13) to determine the ^{2}H$(p,\gamma)^3$He reaction rate in the $E_{c.m.}<1$ keV region. Since the current results (solid line in Fig. 13) show a significant lowering of the the S factor in this region, it is interesting to explore the possible ramifications concerning the conclusions of this protostellar calculation. If we make the reasonable assumption that changes in the ^{2}H$(p,\gamma)^3$He S factor will scale as changes in the interstellar deuterium concentration [42], we can then use the results presented in Ref. [11], which gauge the effect of varying the interstellar deuterium concentration, to estimate the effect of varying the ^{2}H$(p,\gamma)^3$He S factor.

The primary conclusions of Ref. [11], which consist of predictions for the observed temperature and luminosity of developing protostars, are based on an interstellar deuterium-to-hydrogen ratio (D/H) of 2.5×10^{-5}. However, Fig. 6 in Ref. [11] shows the effect on the calculation of varying D/H over a large range. It can be seen from this figure that a 50% reduction in D/H (equivalent to a 50% reduction in the ^{2}H$(p,\gamma)^3$He S factor with D/H constant) leads to a significant change in the mass-radius relation of the developing protostellar core. Rather than continuing to expand with accreted mass, the stellar core now halts expansion at around 0.7 solar masses, and, in fact, begins to contract. This contraction should ruin the ''thermostat effect'' mentioned earlier, and thus could have a significant influence on the observed temperature and luminosity of the star. The effect of a 35% reduction in the ^{2}H$(p,\gamma)^3$He S factor (which is the result of the current experimental study), as compared with the 50% reduction discussed above, is not clear. One can speculate, however, that noticeable changes in the calculation might still result.

ACKNOWLEDGMENTS

We greatly appreciate the help we received during this experiment from all the TUNL staff. We would also like to thank A. Kievsky, R. Schiavilla, and M. Viviani for valuable discussions on the theory of these systems. This work was supported in part by U.S. DOE Grant No. DEFG05-91-ER40619.

[1] G. J. Schmid, R. M. Chasteler, C. M. Laymon, H. R. Weller, R. M. Prior, and D. R. Tilley, Phys. Rev. C **52**, R1732 (1995).

[2] G. J. Schmid *et al.*, Phys. Rev. Lett. **76**, 3088 (1996).

[3] G. J. Schmid, R. M. Chasteler, C. M. Laymon, H. R. Weller, R. M. Prior, and D. R. Tilley, Nucl. Phys. **A607**, 139 (1996).

[4] J. L. Friar, B. F. Gibson, H. C. Jean, and G. L. Payne, Phys. Rev. Lett. **66**, 1827 (1991).

[5] A. Kievsky, M. Viviani, and S. Rosati, Nucl. Phys. **A557**, 511 (1994).

[6] J. Torre and B. Goulard, Phys. Rev. C **28**, 529 (1983).

[7] J. L. Friar, B. F. Gibson, and G. L. Payne, Phys. Lett. B **251**, 11 (1990).

[8] L. I. Schiff, Phys. Rev. **52**, 242 (1937).

[9] M. Verde, Helv. Phys. Acta **23**, 453 (1950).

[10] C. E. Rolfs and W. S. Rodney, *Cauldrons in the Cosmos* (University of Chicago Press, Chicago, 1988).

[11] S. W. Stahler, Astrophys. J. **322**, 804 (1988).

[12] G. M. Griffiths, M. Lal, and C. D. Scarfe, Can. J. Phys. **41**, 724 (1963).

[13] G. M. Bailey, G. M. Griffiths, M. A. Olivio, and R. L. Helmer, Can. J. Phys. **48**, 3059 (1970).

[14] D. H. Wilkinson, Philos. Mag. **43**, 659 (1952).

[15] T. B. Clegg, Rev. Sci. Instrum. **61**, 385 (1990).

[16] G. J. Schmid, Ph.D. thesis, Duke University, 1995.

[17] The TUNL XSYS data acquisition system, Triangle Universities Nuclear Laboratory, Durham, NC.

[18] D. A. Andrews and G. Newton, J. Phys. D **10**, 845 (1977).

[19] W. A. Wenzel and W. Whaling, Phys. Rev. **87**, 499 (1952).

[20] W. Whaling and W. A. Wenzel, Phys. Rev. **85**, 761A (1952).
[21] H. H. Anderson and J. F. Ziegler, *Hydrogen Stopping Powers* (Pergamon, New York, 1977).
[22] D. I. Thwaits, Nucl. Instrum. Methods Phys. Res. B **12**, 84 (1985).
[23] D. I. Thwaits, Nucl. Instrum. Methods Phys. Res. B **69**, 53 (1992).
[24] Y. J. Xu, G. S. Khandelwal, and J. W. Wilson, Phys. Rev. A **32**, 629 (1985).
[25] C. Mitterschiffthaler and P. Bauer, Nucl. Instrum. Methods Phys. Res. B **48**, 58 (1990).
[26] H. H. Baarschall and W. Haeberli, *Polarization Phenomena in Nuclear Reactions* (University of Wisconsin Press, Madison, Wisconsin, 1971).
[27] W. S. Wilburn, Ph.D. thesis, Duke University, 1993.
[28] R. G. Seyler and H. R. Weller, Phys. Rev. C **20**, 453 (1979).
[29] A. E. Litherland, G. T. Ewan, and S. T. Lam, Can. J. Phys. **48**, 2320 (1970).
[30] J. R. Williams, Ph.D. thesis, North Carolina State University, 1974.
[31] W. R. Nelson, H. Hirayama, and D. W. O. Rogers, The EGS4 code, SLAC Report 265, 1985.
[32] F. James and M. Roos, MINUIT, CERN Computer Centre Program Library, 1977.
[33] M. E. Rose, Phys. Rev. **91**, 610 (1953).
[34] M. Viviani, R. Schiavilla, and A. Kievsky, Phys. Rev. C **54**, 534 (1996).
[35] A. Arriaga and F. D. Santos, Phys. Rev. C **39**, 1945 (1984).
[36] M. C. Vetterli, J. A. Kuehner, A. J. Trudel, C. L. Woods, R. Dymarz, A. A. Pilt, and H. R. Weller, Phys. Rev. Lett. **54**, 1129 (1985).
[37] M. C. Vetterli, Ph.D. dissertation, McMaster University, 1985.
[38] B. F. Gibson and D. R. Lehman, Phys. Rev. C **29**, 1017 (1984).
[39] B. J. Rice and H. R. Weller, Phys. Rev. C **55**, 2700 (1997).
[40] Z. Ayer, H. J. Karwowski, B. Kozlowska, and E. J. Ludwig, Phys. Rev. C **52**, 2851 (1995).
[41] J. L. Friar, B. F. Gibson, D. R. Lehman, and G. L. Payne, Phys. Rev. C **37**, 2859 (1988).
[42] S. W. Stahler (private communication).